Dielectric function of *a*-Si:H based on local network structures

Shota Kageyama, Masataka Akagawa, and Hiroyuki Fujiwara[*]
Center of Innovative Photovoltaic Systems (CIPS), Gifu University, 1-1 Yanagido, Gifu 501-1193, Japan

(Received 16 December 2010; revised manuscript received 21 March 2011; published 5 May 2011)

For hydrogenated amorphous silicon (*a*-Si:H) layers prepared by plasma-enhanced chemical vapor deposition, we have found clear relationships between the dielectric function in the ultraviolet/visible region and SiH_n (n = 1–2) local bonding states by applying real-time spectroscopic ellipsometry and infrared attenuated total reflection spectroscopy. In particular, the amplitude of the ε_2 spectra obtained from various *a*-Si:H layers is expressed completely by the SiH_2 bond density in the *a*-Si:H and reduces strongly with increasing the SiH_2 content, indicating that microvoids present in the *a*-Si:H network are surrounded by the SiH_2 bonding state. On the other hand, no significant void formation occurs by the generation of the SiH local bonding due to rather dense surrounding structures. Depending on the SiH_n bonding states, the whole *a*-Si:H dielectric function shifts toward higher energies, as the SiH_n hydrogen contents in the *a*-Si:H increase. Based on these findings, we have established a new *a*-Si:H dielectric function model that incorporates the void structure terminated with SiH_2 and ε_2 spectral shift induced by the SiH_n local structures. This model is appropriate for a wide variety of *a*-Si:H layers deposited at different substrate temperatures and plasma conditions and, conversely, allows the characterization of the SiH_n contents from the *a*-Si:H dielectric functions in the ultraviolet/visible region. From results obtained in this study, the local network structures and electronic states of *a*-Si:H are discussed.

DOI: 10.1103/PhysRevB.83.195205 PACS number(s): 78.20.Ci, 78.66.Jg, 81.05.Gc, 71.23.Cq

I. INTRODUCTION

The network structure of hydrogenated amorphous silicon (*a*-Si:H) thin films and the resulting optoelectronic properties have long been a subject of intense discussion[1] since the first demonstration of *p*,*n*-type conductivity control in *a*-Si:H by Spear and Le Comber.[2,3] Although a continuous random network is generally assumed for *a*-Si:H,[4–8] the optoelectronic properties of *a*-Si:H are unique and depend strongly on H incorporated in the amorphous network.[9–18] More specifically, the band-edge absorption of *a*-Si:H shifts toward higher energies with increasing the total hydrogen content (C_{total}) in *a*-Si:H.[9,10] Thus H introduced during *a*-Si:H growth processes not only passivates Si dangling bonds but also modifies the fundamental properties of *a*-Si:H.[1]

Several studies have shown that, when H is incorporated into *a*-Si:H, deformation of the network structure occurs with the generation of microvoids in the *a*-Si:H matrix.[19–27] Unfortunately, there has been little consensus on the detailed void structures in *a*-Si:H and various *a*-Si:H void structures have been reported from different characterization techniques including small-angle x-ray scattering (SAXS),[19–21] neutron scattering,[22] positron annihilation,[23,24] infrared spectroscopy (IR),[25,26] and nuclear magnetic resonance (NMR).[27] One of the controversies over the void structure in *a*-Si:H arises from the internal surface structure of microvoids. In general, such void surfaces present in *a*-Si:H layers are considered to be terminated with SiH_n (n = 1–2) bonding states,[25,26] but the interpretation of IR[25,26,28–34] and NMR[27,35–40] results is still highly controversial. Moreover, the size of the microvoids in *a*-Si:H varies depending on *a*-Si:H preparation conditions as well as characterization techniques, and the diameter of voids has been reported to be ∼8 Å (SAXS),[19,20] ∼20 Å (positron annihilation[23] and NMR[27]), and >20 Å (SAXS[21] and neutron scattering[22]).

The microvoid formation in the *a*-Si:H network is expected to change optical constants and dielectric function of *a*-Si:H in the visible/ultraviolet (UV) region. As known widely, the *a*-Si:H dielectric function, $\varepsilon_{a\text{-Si:H}}(E) = \varepsilon_1(E) - i\varepsilon_2(E)$, shows a broad feature with a single ε_2 peak at E = 3.6 eV.[11,12,41] This ε_2 peak basically shows the fundamental light absorption in *a*-Si:H,[41] and thus provides a measure of the material density in *a*-Si:H. Accordingly, the *a*-Si:H network structure with microvoids and its relation to the optical transitions can best be investigated from $\varepsilon_{a\text{-Si:H}}(E)$. In fact, the ε_2 spectra of *a*-Si:H have been reported to vary systematically with C_{total}, and the amplitude of the ε_2 peak reduces at higher C_{total}.[11,12] The relationships between $\varepsilon_{a\text{-Si:H}}(E)$ and SiH_n local bonding structures can be related to the microvoid structures in the *a*-Si:H network.

To express $\varepsilon_{a\text{-Si:H}}(E)$, on the other hand, various dielectric function models, including the Forouhi-Bloomer model,[42] model dielectric function theory,[43] band model,[44] tetrahedral model,[45,46] Tauc-Lorentz model,[47] and Cody-Lorentz model,[48] have been proposed. In the Tauc-Lorentz model that has been applied extensively, the dielectric function is described by five independent parameters, namely, amplitude parameter, broadening parameter, band gap, and peak position of an ε_2 peak, and an ε_1 value at high energies.[47] Although dielectric function modeling with such parameters is suitable to express the optical constants of various amorphous materials, the assessment of film quality becomes rather difficult from such models. In the case of *a*-Si:H, for example, the SiH_2 bonding mode, generally characterized by the ∼2080 cm^{-1} peak in IR spectra, has been an important indicator for *a*-Si:H film quality, as light-induced degradation that occurs in the solar cell devices shows a good correlation with the generation of the SiH_2 bonding state in *a*-Si:H.[14–18] For the *a*-Si:H solar cell application, therefore, it is of significant importance to develop an *a*-Si:H dielectric function model that allows the characterization of the SiH_2 bonding state.

In this study, we have investigated the relationships between $\varepsilon_{a\text{-Si:H}}(E)$ in the visible/UV region and SiH_n local bonding

 ©2011 American Physical Society

states. The amplitude of $\varepsilon_{a\text{-Si:H}}(E)$ is found to show a direct correlation with the SiH_2 bond formation in *a*-Si:H, indicating that microvoids in the *a*-Si:H network are terminated by the SiH_2 bonds, while the SiH bonding state is present in rather dense network structures. These SiH and SiH_2 local structures induce the ε_2 spectral shifts toward higher energies with different shift values, as the SiH and SiH_2 bond densities in the *a*-Si:H increase. As a result, we have developed a dielectric function model based on the *a*-Si:H local network structures.

II. EXPERIMENT

We prepared *a*-Si:H layers by a conventional rf plasma-enhanced chemical vapor deposition (PECVD) system. This PECVD system is equipped with real-time spectroscopic ellipsometry (SE) and infrared attenuated total reflection spectroscopy (ATR).[49] In this study, a series of *a*-Si:H layers were deposited on Si(100) substrates covered with 30-Å-thick native oxides at different substrate temperatures (T_s) ranging from 80 to 310 °C. The calibration of T_s was performed by estimating near-surface temperatures using the reported temperature response of the dielectric function for crystalline silicon (*c*-Si).[50] In the *a*-Si:H depositions, a fixed SiH_4 flow rate of 5 SCCM (SCCM denotes cubic centimeter per minute at STP), an rf power ($P_{\rm rf}$) of 13 mW/cm^2, and a pressure of 50 mTorr were used, and the electrode spacing in the PECVD was 4 cm. These deposition conditions yield a relatively slow *a*-Si:H deposition rate of 0.4 Å/s ($T_s \leqslant 280$ °C). At $T_s = 310$ °C, the deposition rate increases to 0.5 Å/s due to H desorption from the *a*-Si:H growing surface.[51] The thickness of the *a*-Si:H layers deposited on the substrates is 1000 Å. For the *a*-Si:H depositions at high temperatures, however, the *a*-Si:H thickness was reduced to 300 Å ($T_s = 230$, 280 °C) and 200 Å ($T_s = 310$ °C), as the thick *a*-Si:H layers deposited at high T_s peeled off from the substrates due to the high compressive stresses in these layers.[52]

During the *a*-Si:H depositions, the real-time SE and ATR spectra were measured simultaneously. The SE measurements were performed using a rotating-compensator instrument (J. A. Woollam, M-2000). The real-time SE spectra were collected with a measurement repetition time of 10 s in photon energies ranging from 1.7 to 5.0 eV. We also performed *ex situ* SE measurements using a rotating-analyze ellipsometry instrument with a compensator (J. A. Woollam, VASE), in order to extend the SE measurement region from 0.75 to 5.0 eV.

The real-time ATR spectra were measured by employing a Fourier-transform IR instrument (Nicolet, Magna 560) with a repetition time of 30 s. At $T_s = 280$–310 °C, a longer repetition time of 60 s was used due to lower measurement sensitivity at high T_s. For the ATR measurements, trapezoidal *c*-Si ATR prisms with a size of $80 \times 20 \times 1$ mm^3 were employed. The total number of reflection on an effective surface area of 60×20 mm^2 is 30, which provides quite high sensitivity for the measurements.[49] In the ATR measurements, we eliminated unfavorable interference effects induced by the *a*-Si:H/SiO_2/*c*-Si structure by irradiating *p*-polarized IR light into the ATR prism.[49] The measurement of the ATR spectra was performed using a spectra resolution of 8 cm^{-1} in a wave-number range from 1500 to 4000 cm^{-1}. In our case, the lowest measurable range in the ATR spectra is limited by the onset of the strong absorption of the *c*-Si ATR prism.

III. SE AND ATR ANALYSES

For the analysis of real-time SE spectra, we constructed an optical model of multiple layers consisting of ambient/surface roughness layer (*a*-Si:H)/bulk layer (*a*-Si:H)/SiO_2 (30 Å)/*c*-Si (substrate).[53] The dielectric function of the surface roughness layer was modeled as a 50/50 vol.% mixture of the *a*-Si:H bulk layer and voids, applying the Bruggeman effective-medium approximation (EMA).[53,54] In order to determine $\varepsilon_{a\text{-Si:H}}(E)$ deposited at different T_s, a global error minimization scheme was used. In this method, the overall analysis is made self-consistently under the assumption that the dielectric function of the depositing film does not change within the analyzing film thickness.[53,54] This analysis allows us to obtain a time evolution of the surface roughness layer thickness (d_s), bulk layer thickness (d_b), in addition to the dielectric function of the film. From the analysis, however, $\varepsilon_{a\text{-Si:H}}(E)$ at T_s is determined. The $\varepsilon_{a\text{-Si:H}}(E)$ at room temperature can be extracted from the room-temperature SE spectra measured after the *a*-Si:H deposition. In this case, the mathematical inversion of the room-temperature spectra is performed assuming that d_s and d_b of the *a*-Si:H layer do not vary after the *a*-Si:H deposition.[54] In our analysis, however, slight adjustments for d_s and d_b were made for the mathematical inversion to remove artifacts from the dielectric function. On the other hand, the SE spectra at the lower energy region (0.75−1.7 eV) were obtained from the *ex situ* measurements mentioned earlier. These *ex situ* spectra, however, include the effect of *a*-Si:H oxidation that occurs after removing the sample from the deposition system. We have removed this oxidation effect by introducing additional surface roughness and/or SiO_2 contributions into the optical model, so that $\varepsilon_{a\text{-Si:H}}(E)$ obtained from the *ex situ* measurement matches with the one determined from the *in situ* measurement. Finally, by combining the *ex situ* and *in situ* results, $\varepsilon_{a\text{-Si:H}}(E)$ in a range from 0.75 to 5.0 eV was determined.

The data analysis procedure for the real-time ATR spectra has already been established previously.[49] From the measured ATR absorbance spectra $A(\omega)$, where ω denotes the wave number, the absorption coefficient $\alpha(\omega)$ can be calculated directly using

$$\alpha(\omega) = 2.303 \times A(\omega)\mathrm{Re}(\cos\theta)/(2dM). \tag{1}$$

Here, θ denotes the transmission angle of the IR light in thin films formed on ATR prisms, and θ can be obtained easily by applying Snell's law. In Eq. (1), d and M represent the layer thickness and total number of the light reflection on the film side ($M = 30$ in our case), respectively. From SE results, we obtained d as $d = d_b + 0.5d_s$, where the coefficient of 0.5 for d_s indicates 50 vol.% of voids assumed for d_s. From $\alpha(\omega)$ in Eq. (1), the hydrogen content C_H for each SiH_n bonding mode in *a*-Si:H can be estimated as follows:

$$C_H = \frac{A}{D}\left(\int \frac{\alpha(\omega)}{\omega} d\omega\right) \times 100 \text{ at.\%}, \tag{2}$$

where A is a proportionality constant of the SiH_n bonding states and D is the atomic number density of *a*-Si:H.[49] In this study, two IR peaks generally observed at

~2000 cm^{-1} and ~2080 cm^{-1} are assigned to the SiH and SiH_2 stretching modes, respectively, as will be discussed in Sec. VA. For the calculation of the SiH_n contents, we applied values of $D = 5.0 \times 10^{22}$ cm^{-3}, $A_{SiH} = 9.0 \times 10^{19}$ cm^{-2}, and $A_{SiH_2} = 2.2 \times 10^{20}$ cm^{-2}, based on the result reported by Langford *et al.*[55] By applying A_{SiH} and A_{SiH_2} to Eq. (2), the SiH content (C_{SiH}) and SiH_2 content (C_{SiH_2}) in the *a*-Si:H layers were estimated. From these values, we further obtained C_{total} as $C_{total} = C_{SiH} + C_{SiH_2}$.

In the *a*-Si:H deposition on the SiO_2/*c*-Si substrates, on the other hand, a SiH_2-rich interface layer with a thickness of ~30 Å is formed on the substrate due to the island growth of *a*-Si:H on foreign substrates.[56] This interface layer has a quite large C_{SiH_2} of ~20 at.% and provides a constant contribution to the measured ATR spectra.[56] In the SE measurement, however, the optical response of the thin interface layer becomes negligible as the *a*-Si:H layer thickness increases, since the light reflection from the *a*-Si:H/substrate interface region becomes weaker. Thus we have eliminated the contribution of the SiH_2-rich interface layer by subtracting a real-time ATR spectrum obtained during the initial growth regime from a real-time ATR spectrum obtained after the *a*-Si:H deposition, in order to investigate the correlation between $\varepsilon_{a\text{-Si:H}}(E)$ and the SiH_n local bonding states, particularly in the *a*-Si:H bulk layer. The resulting ATR spectrum was then analyzed to estimate the SiH_n content in the *a*-Si:H bulk layer.

IV. RESULTS

A. Dielectric functions of *a*-Si:H

Figure 1 shows the room-temperature dielectric functions of the *a*-Si:H layers deposited at different T_s from 80 to 310 °C. As confirmed from Fig. 1, the ε_1 spectra in Fig. 1(a) and ε_2 spectra in Fig. 1(b) show relatively large variations with T_s. In particular, the overall ε_1 values and the amplitude of the broad ε_2 peak at 3.6 eV decrease as T_s reduces. Moreover, it can be seen that the whole dielectric function shifts toward higher energies with decreasing T_s. At $T_s \geqslant 280$ °C, however, the amplitude of the ε_2 peak is constant and only the slight ε_2-spectral shift occurs, as shown in Fig. 1(c).

Since the dielectric function $\varepsilon(E) = \varepsilon_1(E) - i\varepsilon_2(E)$ is expressed by $\varepsilon_1(E) = n(E)^2 - k(E)^2$ and $\varepsilon_2(E) = 2n(E)k(E)$, where n and k are the refractive index and extinction coefficient, respectively, the ε_2 spectra in Fig. 1(b) basically show the light absorption properties in *a*-Si:H. Thus the result of Fig. 1(b) indicates that the fundamental light absorption in the *a*-Si:H reduces at lower T_s, as reported previously.[11] In addition, the onset of the light absorption ($\varepsilon_2 > 0$) at lower energies around 1.7 eV roughly corresponds to the optical gap of *a*-Si:H. Accordingly, the shift of the absorption onset in Fig. 1(b) indicates the optical gap widening in the *a*-Si:H with decreasing T_s. At energies well below the light absorption regime, on the other hand, $\varepsilon_1(E)$ shows a constant value, referred to as the high-frequency dielectric constant ε_∞.[54] From ε_∞, the high-frequency refractive index n_∞ can be estimated from $\varepsilon_\infty = n_\infty^2$, since $k = 0$ in the region. As shown in Fig. 1(a), the constant ε_1 value at $E < 1.0$ eV reduces with decreasing T_s, indicating that n_∞ reduces at lower T_s by the formation of porous *a*-Si:H network structures.

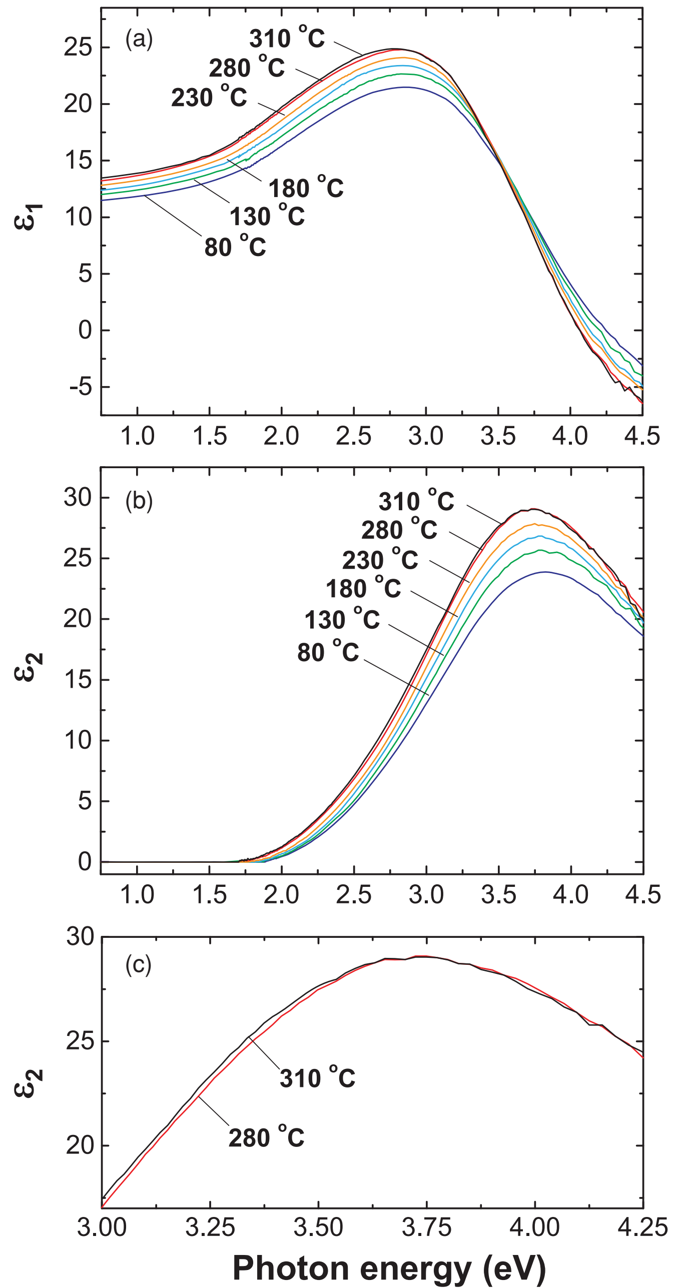

FIG. 1. (Color online) (a) ε_1 spectra, (b) ε_2 spectra of the *a*-Si:H layers deposited at different substrate temperatures of T_s = 80–310 °C, and (c) ε_2 spectra of the *a*-Si:H for T_s = 280 and 310 °C in the selected energy region.

The obtained $\varepsilon_{a\text{-Si:H}}(E)$ in Fig. 1 was further analyzed using the Tauc-Lorentz model.[47] In this model, the $\varepsilon_2(E)$ of amorphous materials is expressed by the product of the Tauc gap and Lorentz model:

$$\varepsilon_2(E) = \frac{ACE_0(E - E_g)^2}{\left(E^2 - E_0^2\right)^2 + C^2E^2}\frac{1}{E} \quad (E > E_g), \tag{3}$$

$$= 0 \quad (E \leqslant E_g), \tag{4}$$

where A, C, E_0, and E_g represent the amplitude parameter, broadening parameter, peak transition energy, and Tauc optical

gap. The $\varepsilon_1(E)$ of the Tauc-Lorentz model has been obtained using the Kramers-Kronig relations and is given by

$$\begin{aligned}\varepsilon_1(E) = \varepsilon_1(\infty) + \frac{AC}{\pi\xi^4}\frac{a_{\ln}}{2\alpha E_0}\ln\left(\frac{E_0^2+E_g^2+\alpha E_g}{E_0^2+E_g^2-\alpha E_g}\right) \\ - \frac{A}{\pi\xi^4}\frac{a_{\tan}}{E_0}\left[\pi - \tan^{-1}\left(\frac{2E_g+\alpha}{C}\right)\right. \\ \left. + \tan^{-1}\left(\frac{-2E_g+\alpha}{C}\right)\right] + 2\frac{AE_0}{\pi\xi^4\alpha}E_g(E^2-\gamma^2) \\ \times\left[\pi + 2\tan^{-1}\left(2\frac{\gamma^2-E_g^2}{\alpha C}\right)\right] - \frac{AE_0C}{\pi\xi^4}\frac{E^2+E_g^2}{E} \\ \times \ln\left(\frac{|E-E_g|}{E+E_g}\right) + \frac{2AE_0C}{\pi\xi^4}E_g \\ \times \ln\left[\frac{|E-E_g|(E+E_g)}{\sqrt{(E_0^2-E_g^2)^2+E_g^2C^2}}\right],\end{aligned} \quad (5)$$

where

$$a_{\ln} = \left(E_g^2 - E_0^2\right)E^2 + E_g^2C^2 - E_0^2\left(E_0^2 + 3E_g^2\right), \quad (6)$$

$$a_{\tan} = (E^2 - E_0^2)(E_0^2 + E_g^2) + E_g^2C^2, \quad (7)$$

$$\xi^4 = (E^2-\gamma^2)^2 + \alpha^2C^2/4, \quad (8)$$

$$\alpha = \sqrt{4E_0^2 - C^2}, \quad (9)$$

$$\gamma = \sqrt{E_0^2 - C^2/2}. \quad (10)$$

The $\varepsilon_1(\infty)$ in Eq. (5) shows the energy-independent contribution to ε_1 at high energies. As a result, the dielectric function by the Tauc-Lorentz model is described by five parameters $\{A, C, E_g, E_0, \varepsilon_1(\infty)\}$.

Figure 2 shows $\varepsilon_{a\text{-Si:H}}(E)$ of $T_s = 310\,^\circ$C. The solid lines in the figure indicate the calculation result obtained by applying the Tauc-Lorentz model, and a good fitting to the experimental data can be seen in the whole measured region. Table I summarizes the Tauc-Lorentz parameters determined from similar analyses performed for the *a*-Si:H layers shown in Fig. 1. In this analysis, we used fixed $C = 2.33$ eV, as this value shows a minor variation with T_s. In Table I, C_{SiH} and $C_{\mathrm{SiH_2}}$ in the *a*-Si:H layers, obtained from ATR analyses described in Sec. IV B, are also shown. Figure 3 shows the variation of the Tauc-Lorentz parameters $\{A, E_g, E_0, \varepsilon_1(\infty)\}$ with C_{total} in the *a*-Si:H. With increasing C_{total}, the parameter A gradually reduces. This variation simply shows the amplitude reduction observed in the ε_2 spectra in Fig. 1(b). The linear variations of E_g and E_0 in Fig. 3 correspond to the shift of $\varepsilon_{a\text{-Si:H}}(E)$ toward higher energies with increasing C_{total} (or decreasing T_s). The increase in $\varepsilon_1(\infty)$ indicates the baseline shift of the ε_1 spectrum with C_{total}. From the result shown in Fig. 3, the dielectric function modeling of *a*-Si:H can be performed to some extent. Nevertheless, the application area of the model is rather limited, as *a*-Si:H properties are represented simply by C_{total} in this case.

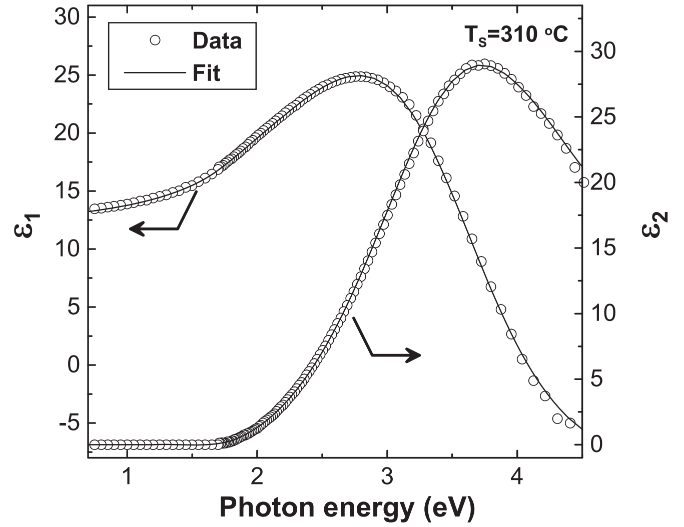

FIG. 2. Dielectric function of the *a*-Si:H layer for $T_s = 310\,^\circ$C. The open circles show the experimental data shown in Fig. 1, and the solid lines show the result of the fitting analysis using the Tauc-Lorentz model.

B. SiH$_n$ local bonding structures

Figure 4 shows the IR absorption spectra of the *a*-Si:H layers for (a) $T_s = 130\,^\circ$C and (b) $T_s = 80$–$310\,^\circ$C. The absorption spectra in Fig. 4 have been obtained using Eq. (1). We analyzed all the ATR spectra assuming the four Gaussian peaks shown in Fig. 4(a). As mentioned earlier, the IR peaks at $\sim$2000 cm^{-1} and $\sim$2080 cm^{-1} have been assigned to SiH and SiH$_2$ stretching modes, respectively. In the ATR analyses, we also included the weak IR peaks observed at $\sim$2180 cm^{-1} and $\sim$2250 cm^{-1} that are assigned to SiH$_2$(O$_2$) and SiH(O$_3$)

TABLE I. Tauc-Lorentz parameters extracted from the fitting analysis of the *a*-Si:H dielectric functions shown in Fig. 1 and SiH$_n$ hydrogen contents deduced from Fig. 4(b).

	Tauc-Lorentz parameters[a]				Hydrogen contents	
Substrate temperature T_s (°C)	A (eV)	E_g (eV)	E_0 (eV)	$\varepsilon_1(\infty)$	C_{SiH} (at.%)	$C_{\mathrm{SiH_2}}$ (at.%)
80	199.37	1.744	3.673	0.920	8.7 ± 0.3	13.1 ± 0.6
130	207.94	1.717	3.670	0.597	8.9 ± 0.3	8.3 ± 0.6
180	211.90	1.688	3.656	0.440	9.0 ± 0.3	6.1 ± 0.6
230	214.05	1.659	3.649	0.309	8.0 ± 0.3	3.6 ± 0.6
280	217.98	1.627	3.637	0.073	7.1 ± 0.3	1.1 ± 0.6
310	217.28	1.614	3.626	0.080	5.4 ± 0.3	1.1 ± 0.6

[a] $C = 2.33$ eV (fixed).

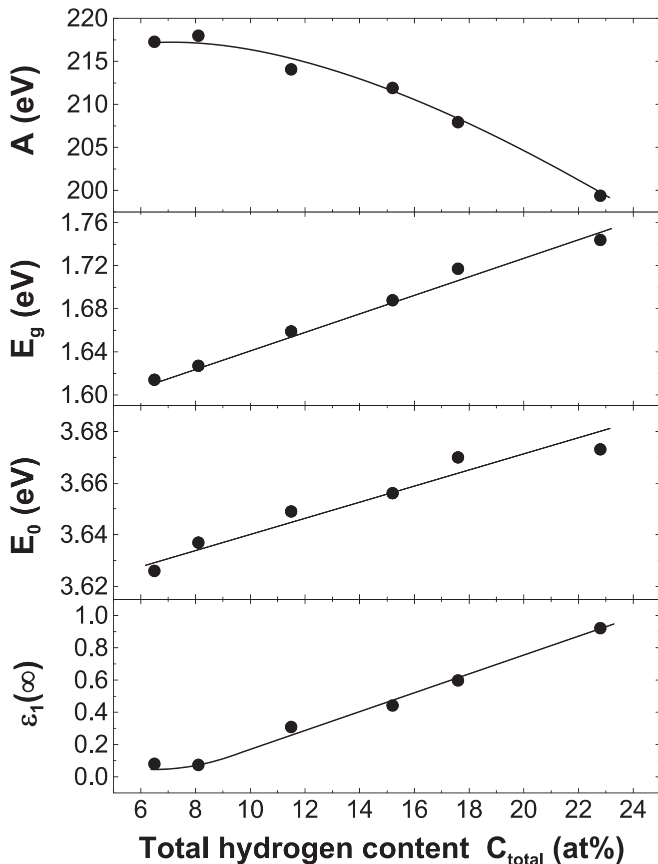

FIG. 3. Tauc-Lorentz parameters extracted from the a-Si:H dielectric functions in Fig. 1, plotted as a function of the total hydrogen content C_{total} in the a-Si:H layers.

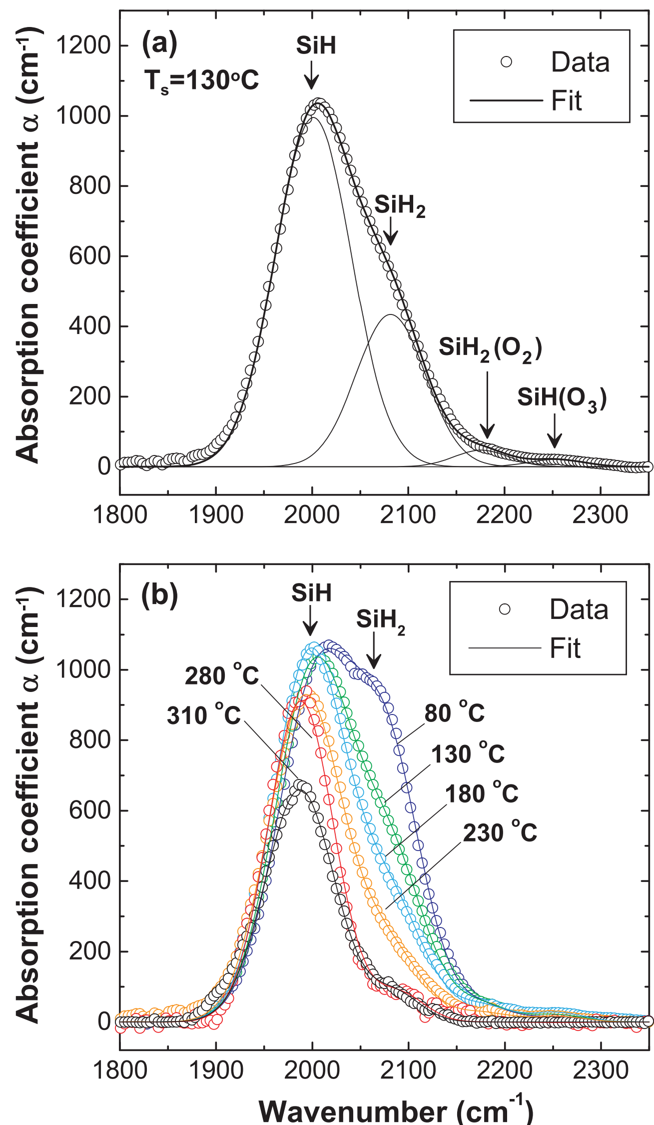

FIG. 4. (Color online) IR absorption spectra of the a-Si:H layers for (a) $T_s = 130\,^\circ$C and (b) $T_s = 80$–$310\,^\circ$C. The solid lines show the results of the peak deconvolution analyses using the four Gaussian peaks in (a).

bonding states, respectively.[57,58] As shown in Fig. 4(a), the total sum of the four peaks, indicated by the thick solid line, provides a good fitting to the measured ATR spectrum. The solid lines in Fig. 4(b) also show the result of the ATR analyses performed for the other a-Si:H layers.

In Fig. 4(b), the SiH_2 absorption peak decreases drastically with increasing T_s and becomes constant at $T_s \geqslant 280\,^\circ$C, while the SiH peak shows a moderate variation. The peak position of the SiH bonding mode shifts slightly toward lower wave numbers. This is primarily caused by the variation of the measurement temperature, since the ATR spectra shown in Fig. 4 were obtained at the a-Si:H deposition temperatures. As reported previously,[59] both SiH and SiH_2 peaks shift toward lower wave numbers with increasing the measurement temperature. In this study, the real-time spectra have been used for the analysis to remove the contribution of the SiH_2 interface layer described in Sec. III.

Figure 5 shows C_{SiH} and C_{SiH_2} estimated from the ATR spectra in Fig. 4(b), plotted as a function of T_s. The actual values in Fig. 5 have been shown in Table I. In Fig. 5 and Table I, the confidence limits for C_{SiH} and C_{SiH_2} determined from the Gaussian peak fitting are shown. As confirmed from Fig. 5, with increasing T_s, C_{SiH_2} reduces strongly up to $T_s = 280\,^\circ$C and shows a constant value of 1.1 at.% above $280\,^\circ$C. On the other hand, C_{SiH} is constant at ∼9 at.% in the low-temperature region ($T_s \leqslant 180\,^\circ$C), and decreases gradually at $T_s \geqslant 230\,^\circ$C. A similar variation of the SiH_n contents versus T_s has been reported previously.[60] The result in Fig. 5 indicates clearly that H desorption during the a-Si:H growth occurs predominantly from H-rich structures that lead to the SiH_2 bond formation at $T_s < 280\,^\circ$C, whereas the SiH bonding state is more thermally stable.

C. Dielectric function model

From the results described above, we have established a dielectric function model based on the a-Si:H local network structures. In particular, we find that the amplitude of the a-Si:H ε_2 peak is described completely by C_{SiH_2} in the a-Si:H layer. Figure 6 shows (a) the ε_2 peak value of $\varepsilon_{a\text{-Si:H}}(E)$ in Fig. 1 and (b) n_∞, plotted as a function of C_{SiH_2} in the a-Si:H layer. The ε_2 peak value in Fig. 6(a) simply represents the ε_2 value at the peak position around 3.6 eV, while n_∞ in

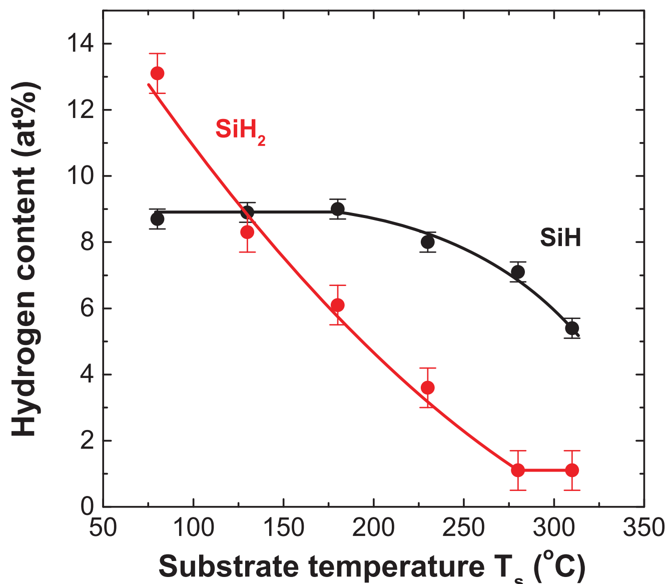

FIG. 5. (Color online) SiH and SiH_2 contents in the a-Si:H layers, plotted as a function of the substrate temperature for the a-Si:H deposition.

Fig. 6(b) shows n at ~0 eV estimated from the Tauc-Lorentz parameters in Table I. It can be seen that the ε_2 peak value reduces quite linearly with increasing C_{SiH_2}. This relationship can be confirmed easily by comparing the amplitude of the ε_2 peaks in Fig. 1(b) with C_{SiH_2} in Fig. 5. Specifically, when C_{SiH_2} increases with constant $C_{SiH} \sim 9$ at.% at $T_s \leqslant 180\,^{\circ}$C, the amplitude of the ε_2 spectra reduces strongly. On the contrary, when C_{SiH} changes with constant $C_{SiH_2} = 1.1$ at.% at $T_s \geqslant 280\,^{\circ}$C, there is no variation in the ε_2 peak amplitude. As confirmed from Fig. 6(b), on the other hand, n_∞ of the a-Si:H also decreases linearly with C_{SiH_2}. Quite interestingly, n_∞ of the a-Si:H is higher than that of c-Si ($n_\infty = 3.42$) when $C_{SiH_2} <$ 9 at.%. The higher n_∞ in a-Si:H at low C_{total} has also been confirmed previously.[55,61] The observed increase in n_∞ could be explained by the introduction of additional Si atoms by the ion bombardment in PECVD.

As mentioned earlier, the ε_2 peak shows the fundamental light absorption in a-Si:H. Thus the reduction in the ε_2 peak amplitude strongly suggests the decrease in the a-Si:H film density due to the microvoid formation in the a-Si:H network. Here, we assume that the amplitude of $\varepsilon_{a\text{-Si:H}}(E)$ decreases with increasing C_{SiH_2} by the formation of microvoids terminated with SiH_2 bonds. The reduction in n_∞ with C_{SiH_2} is also consistent with our hypothesis. On the other hand, the ε_2 peak amplitude is rather independent of C_{SiH}. This phenomenon indicates that the SiH bonding state is embedded into dense a-Si:H network structures with no significant void fraction.

From the above hypothesis, we have constructed a new dielectric function model for a-Si:H, further assuming that $\varepsilon_{a\text{-Si:H}}(E)$ in the visible/UV region is determined completely by C_{SiH} and C_{SiH_2}. In particular, $\varepsilon_{a\text{-Si:H}}(E)$ has been modeled by taking into account two important effects; namely, (i) the amplitude reduction of $\varepsilon_{a\text{-Si:H}}(E)$ with C_{SiH_2} due to the SiH_2-microvoid formation, and (ii) the shift of $\varepsilon_{a\text{-Si:H}}(E)$ toward higher energies with increasing C_{SiH} and C_{SiH_2}. In this study,

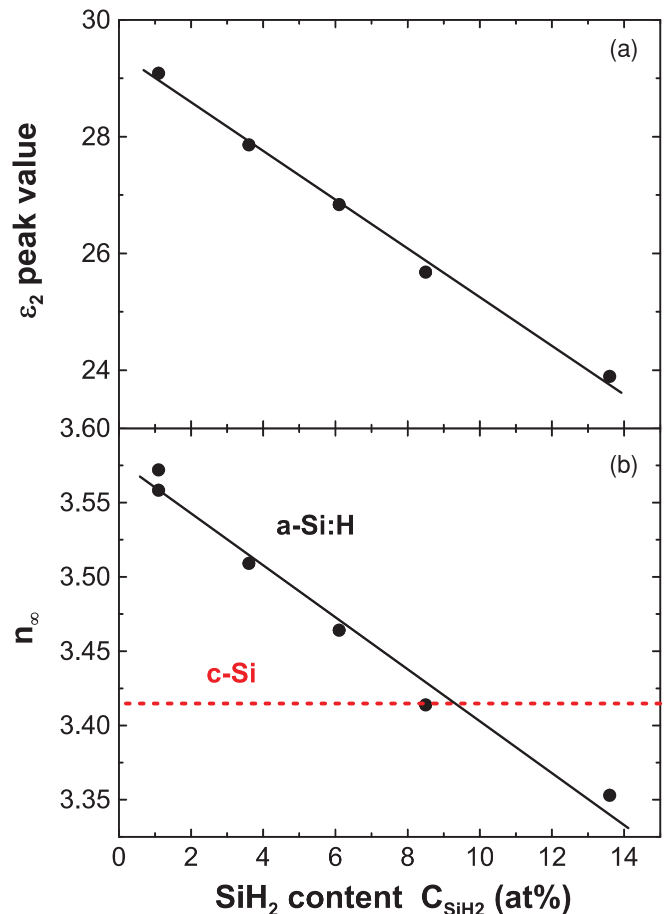

FIG. 6. (Color online) (a) ε_2 peak value and (b) high-frequency refractive index n_∞ of the a-Si:H layers, plotted as a function of the SiH_2 content in the a-Si:H layers.

the formation of the microvoids surrounded by SiH_2 bonds is expressed by applying EMA:

$$f_{a\text{-Si}}\frac{\varepsilon_{a\text{-Si}}(E)-\varepsilon_m(E)}{\varepsilon_{a\text{-Si}}(E)+2\varepsilon_m(E)}+f_{cav}\frac{\varepsilon_{cav}(E)-\varepsilon_m(E)}{\varepsilon_{cav}(E)+2\varepsilon_m(E)}=0, \quad (11)$$

where $\varepsilon_{a\text{-Si}}(E)$ and $\varepsilon_{cav}(E)$ denote the dielectric functions of a-Si without H and SiH_2-microvoid cavity, respectively. It should be noted that $\varepsilon_{cav}(E)$ is not necessary to be $\varepsilon_{cav}(E)$ = 1, as a spherical cavity assumed for the SiH_2 microvoids may include the effect of microscopic atomic configurations. In Eq. (11), $f_{a\text{-Si}}$ and f_{cav} ($f_{a\text{-Si}} + f_{cav} = 1$) represent the volume fractions of the a-Si and microvoid cavity. By solving Eq. (11), the dielectric function of the a-Si network with the SiH_2-microvoid cavity is calculated as $\varepsilon_m(E)$. On the other hand, the shift of $\varepsilon_{a\text{-Si:H}}(E)$ toward higher energies with C_{SiH} and C_{SiH_2} can be confirmed from Figs. 1 and 3. We have modeled the energy shift simply by

$$\varepsilon_{a\text{-Si:H}}(E)=\varepsilon_m(E-\Delta E_{SiH}-\Delta E_{SiH_2}), \quad (12)$$

where ΔE_{SiH} and ΔE_{SiH_2} show the shift values of the dielectric function for C_{SiH} and C_{SiH_2}, respectively.

In our analysis, $\varepsilon_{a\text{-Si}}(E)$ in Eq. (11) was represented by $\varepsilon_{a\text{-Si:H}}(E)$ deposited at $T_s = 310\,^{\circ}$C, since this a-Si:H film shows the lowest H incorporation. To suppress the spectral noise of $\varepsilon_{a\text{-Si:H}}(E)$ for $T_s = 310\,^{\circ}$C, the Tauc-Lorentz

parameters shown in Table I (310 °C) were used. For the actual calculation of $\varepsilon_{a\text{-Si:H}}(E)$ using Eq. (12), however, f_{cav} and $\varepsilon_{\text{cav}}(E)$ in Eq. (11) and ΔE_{SiH} and ΔE_{SiH_2} in Eq. (12) should be determined. Here, we assume that f_{cav}, ΔE_{SiH}, and ΔE_{SiH_2} vary linearly with C_{SiH} or C_{SiH_2}, and are given by

$$f_{\text{cav}} = V_{\text{cav}} \Delta C_{\text{SiH}_2}, \quad (13)$$

$$\Delta E_{\text{SiH}} = k_1 \Delta C_{\text{SiH}}, \quad (14)$$

$$\Delta E_{\text{SiH}_2} = k_2 \Delta C_{\text{SiH}_2}, \quad (15)$$

where V_{cav} shows the volume factor for the SiH_2-microvoid cavity, and k_1 and k_2 indicate the coefficients for the energy shifts, respectively. In Eqs. (13)–(15), ΔC_{SiH} and ΔC_{SiH_2} show the change in C_{SiH} and C_{SiH_2} from the a-Si:H layer deposited at $T_s = 310\,^\circ\text{C}$, and are given by $\Delta C_{\text{SiH}} = C_{\text{SiH}} - 5.4$ at.% and $\Delta C_{\text{SiH}_2} = C_{\text{SiH}_2} - 1.1$ at.%. From C_{SiH} and C_{SiH_2}, therefore, the values of f_{cav}, ΔE_{SiH}, and ΔE_{SiH_2} can be obtained quite easily, if (V_{cav}, k_1, k_2) are known. We have determined these values from the fitting of all the *a*-Si:H dielectric functions obtained at $T_s \leqslant 280\,^\circ\text{C}$. In addition, we assumed $\varepsilon_{\text{cav}}(E)$ as an energy-independent parameter.

Figure 7 shows the dielectric functions of the *a*-Si:H layers deposited at $T_s = 80$–$280\,^\circ\text{C}$. The solid lines in Fig. 7 show the fitting result obtained from the above analysis. As shown in Fig. 7, the calculation result shows almost perfect agreement with the experimental data, supporting the validity of our dielectric function model. From this result, we concluded that the amplitude of $\varepsilon_{a\text{-Si:H}}(E)$ decreases with increasing C_{SiH_2} by the formation of microvoids terminated with SiH_2 bonds. So far, a similar SiH_2-microvoid structure has already been proposed.[25] Nevertheless, our result provides confirmation that the amplitude of $\varepsilon_{a\text{-Si:H}}(E)$ is determined almost completely by the SiH_2-microvoid structure. The parameter values of (V_{cav}, k_1, k_2, ε_{cav}), estimated by minimizing the fitting error, are $V_{\text{cav}} = 1.01$%/at.%, $k_1 = 9.4$ meV/at.%, $k_2 = 4.0$ meV/at.%, and $\varepsilon_{\text{cav}} = 3.5$, respectively. The result of Fig. 7 indicates clearly that the optical properties of *a*-Si:H in the visible/UV region are completely determined by the SiH_n local network structures; in other words, the fundamental *a*-Si:H network structure does not change with the H incorporation, and only the SiH_2-microvoid formation and the energy shift induced by SiH and SiH_2 bonding states occur. If our model is applied, $\varepsilon_{a\text{-Si:H}}(E)$ can be calculated from only two parameters: i.e., C_{SiH} and C_{SiH_2}. Conversely, C_{SiH} and C_{SiH_2} can be extracted from the fitting analysis of experimental $\varepsilon_{a\text{-Si:H}}(E)$. Figure 8 shows the plane view of the *a*-Si:H network structure with the microvoid terminated with SiH_2 and the SiH bonds embedded into the dense network. The network structure of *a*-Si:H will be discussed in Sec. V B.

D. Application of the *a*-Si:H dielectric function model

In order to find the versatility of the above *a*-Si:H-dielectric-function model, we have estimated C_{SiH} and C_{SiH_2} of *a*-Si:H layers deposited with different conditions using our model. Table II summarizes C_{SiH} and C_{SiH_2} of three different *a*-Si:H layers deduced from the SE analyses. For comparison, C_{SiH} and C_{SiH_2} determined from the direct characterization by ATR

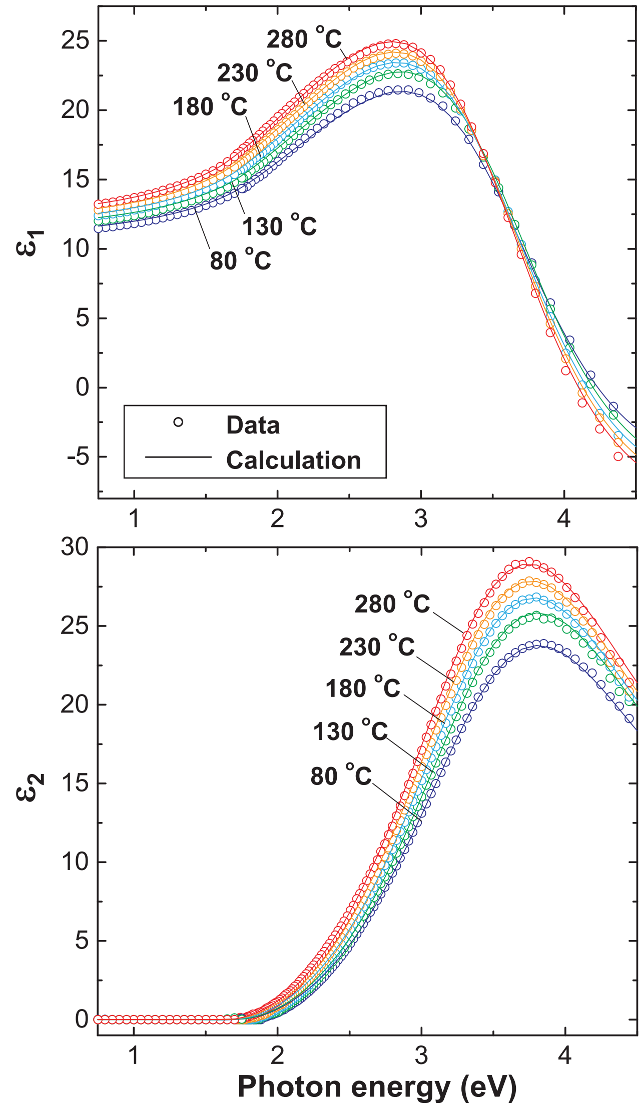

FIG. 7. (Color online) Analysis of the *a*-Si:H dielectric functions for $T_s = 80$–$280\,^\circ\text{C}$. The solid lines represent the result of the fitting analysis using the *a*-Si:H dielectric function model in this study.

are also shown in Table II. The error ranges for the SE analysis in Table II are denoted by the original error ranges in the ATR analysis, as the errors in the ATR deconvolution analysis are much larger than the confidence limits obtained in the SE fitting analyses.

It can be seen from Table II that C_{SiH} and C_{SiH_2} determined by SE and ATR agree quite well. This confirms our conclusion that *a*-Si:H optical properties are determined by the *a*-Si:H local network structures. In general, when P_{rf} is increased, C_{SiH_2} increases, together with the growth rate of *a*-Si:H.[16–18] This increase in C_{SiH_2} at higher P_{rf} is well reproduced in the SE and ATR results in Table II. In the case of sample 3, H_2 gas was introduced into the reactor with a dilution ratio of $[H_2]/[SiH_4] = 10$, and T_s and P_{rf} were varied. Even in this case, C_{SiH} and C_{SiH_2} estimated by SE show good agreement with those determined by ATR. As confirmed from Table II, C_{SiH_2} obtained from SE agrees well with that obtained from ATR with the differences of $\leqslant 0.2$ at.%. For C_{SiH}, however,

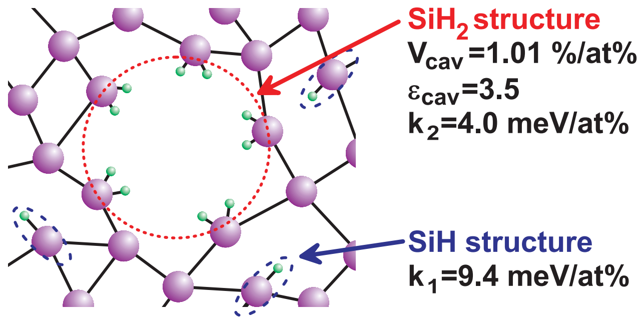

FIG. 8. (Color online) Plane view of the a-Si:H network structure with the SiH_2 microvoid and the SiH structure embedded into the dense Si network.

the difference between the SE and ATR results increases. This originates from the fact that $\varepsilon_{a\text{-Si:H}}(E)$ changes only slightly with C_{SiH} and the sensitivity for C_{SiH} is much lower. In our model, therefore, C_{SiH_2} can be estimated accurately from a large variation in the amplitude of $\varepsilon_{a\text{-Si:H}}(E)$, while C_{SiH} is determined from the energy shift of $\varepsilon_{a\text{-Si:H}}(E)$ with less sensitivity.

As described in Sec. I, the characterization of the SiH_2 bonding state is quite important to deduce the light-induced degradation in a-Si:H solar cells. In the case of the solar cell devices, however, the evaluation of C_{SiH_2} has been rather difficult, as IR light does not transmit glass or stainless-steel substrates on which the solar cells are fabricated. So far, the IR measurement of a-Si:H layers formed on these substrates has been performed by placing an attenuated total reflection (ATR) prism on the substrates.[18] The quantitative analysis of C_{SiH_2} is quite difficult in this case. If the a-Si:H dielectric function model developed in this study is applied, however, C_{SiH_2} in the a-Si:H layers formed on the glass and stainless-steel substrates can be assessed quite easily from the SE analyses.

On the other hand, as confirmed from Table II, our model provides the consistent results for various a-Si:H layers fabricated by different T_s, P_{rf}, and hydrogen dilution. For other a-Si:H layers deposited with quite different growth conditions or techniques, our dielectric function model may show some limitations. Although such limitations have not been found in this study, the application range of our model should be investigated further.

V. DISCUSSION

A. Assignment of IR peaks

Since the beginning of a-Si:H researches, the IR peak observed at ~2000 cm^{-1} has been assigned to the SiH stretching mode vibration,[28–33] while the interpretation of the IR peak observed at ~2080 cm^{-1} has been highly controversial; the peak has been attributed to the different stretching modes of (i) SiH_2 overlapped with SiH_3,[28,31] (ii) SiH_2 overlapped with SiH,[33] (iii) SiH_2 with chainlike $(SiH_2)_n$,[29,30,32] or (iv) clustered SiH.[26,31] Most of the studies reported so far, however, conclude that there is the contribution of the SiH_2 bonding state for the IR peak at ~2080 cm^{-1}. On the other hand, the IR spectra of a-Si:H layers often show a weak IR peak at ~890 cm^{-1}.[28–31] This peak has been assigned to the SiH_2 bending mode unanimously[28,30,32,33] and appears only when the SiH_2 bonding state exists. Recent IR studies show that the integrated absorbance of this SiH_2 bending mode at ~890 cm^{-1} shows almost perfect correlation with that of the ~2080-cm^{-1} peak.[60,62] This fact simply indicates that the IR peak at ~2080 cm^{-1} originates from the SiH_2 stretching mode with no major contributions from other modes. Moreover, as confirmed from Fig. 4, the half width of the ~2080-cm^{-1} peak is essentially similar to that of the SiH stretching mode. If the ~2080-cm^{-1} peak has a contribution other than the SiH_2 stretching mode, the peak width is expected to become much broader. Accordingly, we have assigned the 2080-cm^{-1} peak to the SiH_2 bonding mode.

Previously, on the other hand, the presence of the $(SiH_2)_n$ chain structures in a-Si:H has also been suggested from a sharp IR peak at ~840 cm^{-1}, associated with the wagging mode[29–32] or bending mode.[29,33] For a-Si:H layers deposited by PECVD using SiH_4, the relationship between the ~2080-cm^{-1} and ~840-cm^{-1} peaks is nonlinear, although the integrated absorbance of the ~840-cm^{-1} peak increases with that of the ~2080-cm^{-1} peak.[60] It should be emphasized that the ~840-cm^{-1} peak appears only in specific a-Si:H growth conditions, such as a-Si:H deposition using a Ar and SiH_4 gas mixture[25,28–31,62] and a-Si:H deposition at high growth rates (>1.7 Å/s).[60] In fact, in our a-Si:H layers, the presence of the ~840-cm^{-1} peak has not been confirmed, probably due to the low growth rate of 0.4 Å/s in these layers. In this study, therefore, we have ruled out the possibility of the $(SiH_2)_n$-chain structure formation in the microvoid shown in Fig. 8.

As described in Sec. III, C_{SiH} and C_{SiH_2} have been estimated using proportionality constants of $A_{SiH} = 9.0 \times 10^{19}$ cm^{-2} and $A_{SiH_2} = 2.2 \times 10^{20}$ cm^{-2}.[55] So far, various values have also been reported as the proportionality constants of the SiH_n

TABLE II. SiH_n hydrogen contents in a-Si:H layers obtained from SE and ATR with different growth conditions.

Sample	Growth conditions	Hydrogen contents by SE (at.%)	Hydrogen contents by ATR (at.%)
1	$P_{rf} = 13$ mW/cm^2, $T_s = 180$ °C	$C_{SiH} = 9.0 \pm 0.3$	$C_{SiH} = 9.0 \pm 0.3$
		$C_{SiH_2} = 6.3 \pm 0.6$	$C_{SiH_2} = 6.1 \pm 0.6$
2	$P_{rf} = 38$ mW/cm^2, $T_s = 180$ °C	$C_{SiH} = 9.0 \pm 0.3$	$C_{SiH} = 8.6 \pm 0.3$
		$C_{SiH_2} = 8.1 \pm 0.6$	$C_{SiH_2} = 8.0 \pm 0.6$
3	$P_{rf} = 64$ mW/cm^2, $T_s = 195$ °C,	$C_{SiH} = 9.8 \pm 0.3$	$C_{SiH} = 9.2 \pm 0.3$
	$[H_2]/[SiH_4] = 10$	$C_{SiH_2} = 6.1 \pm 0.6$	$C_{SiH_2} = 6.2 \pm 0.6$

modes.[31,34,63,64] Even if we adopt other values for A_{SiH} and A_{SiH_2}, however, only the coefficients of k_1 and k_2 change and our dielectric function model is still valid. Thus it should be noted that C_{SiH} and C_{SiH_2} and the resulting k_1 and k_2 represent the values when $A_{SiH} = 9.0 \times 10^{19}$ cm^{-2} and $A_{SiH_2} = 2.2 \times 10^{20}$ cm^{-2} are used.

B. *a*-Si:H network structure

As described in Sec. I, several measurement techniques confirmed the formation of the microvoid structures in *a*-Si:H. In particular, the structural studies using SAXS indicate that the microvoid density in *a*-Si:H increases at lower T_s with a constant void size (diameter) of ∼8 Å.[20] Moreover, the microvoid fraction determined by SAXS has been reported to vary linearly with the integrated absorbance of the ∼2080-cm^{-1} peak[20] (or C_{SiH_2} in this study). The above SAXS results are quite consistent with our result. In our model, f_{cav} in the *a*-Si:H increases linearly with C_{SiH_2} ($f_{cav} = V_{cav}\Delta C_{SiH_2}$) with constant $V_{cav} = 1.01$%/at.%. On the contrary, if the microvoid size changes, the relationship between f_{cav} and C_{SiH_2} is expected to become nonlinear. Accordingly, the excellent fitting assuming constant V_{cav} supports the variation in the microvoid density rather than the microvoid size with increasing C_{SiH_2} or decreasing T_s. It should be noted that the void size itself cannot be estimated from the analysis using EMA, as EMA assumes the size-independent optical properties for mixed phase materials.[54] On the other hand, we obtained $\varepsilon_{cav} = 3.5$ ($n_{cav} = 1.87$) from the fitting analysis of Fig. 7. The value of ε_{cav} is larger than 1 and indicates the presence of SiH_2 or Si-Si bonds in the microvoid cavity. So far, it has been reported from IR[65,66] and NMR[27,39,40] measurements that the microvoids in the *a*-Si:H network contain a large amount of H_2 molecules.

Our result shows that the SiH local structure is optically dense and does not introduce additional microvoids. Recently, Smets *et al.* proposed that the SiH bonds exist mainly at vacancy sites, terminating the dangling bonds in the vacancies.[64] Such a SiH structure is consistent with our result, as a small number of the vacancies do not reduce the material density significantly and are not detectable in our analysis. As mentioned earlier, the SiH local structure can be eliminated only at high T_s and is thermally stable. Thus the isolated SiH structure is depicted in Fig. 8, although the clustered SiH at the vacancy sites is still possible.

C. Electronic states of *a*-Si:H

The optical transitions in *a*-Si:H are generally represented by the random network model[67–70] that allows the light absorption with no momentum conservation.[41] Moreover, the ε_2 peak position of ∼ 3.6 eV in *a*-Si:H roughly corresponds to the direct optical transitions at the Γ and Λ points (3.4 eV) and X point (4.3 eV) in *c*-Si.[71] Qualitatively, the broad spectral feature of $\varepsilon_{a\text{-Si:H}}(E)$ can be interpreted by the random optical transitions in the energy-momentum space near the Γ, Λ, and X points in *c*-Si.[41] Thus the optical transition in *a*-Si:H is influenced strongly by the local network structure, and the long-range disorder is not always necessary for the *a*-Si:H modeling.[41,67,69,70,72]

Theoretical calculations performed for *a*-Si:H show that the density of states (DOS) near the valence-band top originates primarily from the Si 3*p* orbital, while the DOS of the conduction-band bottom consists of the mixture of the *s*- and *p*-like orbitals.[70,72] The DOS of the *a*-Si:H valence band has been characterized using x-ray photoelectron spectroscopy (XPS).[41,73] Specifically, von Roedern *et al.* found that the top of the *a*-Si:H valence band shifts toward deeper energy positions as C_{total} in the *a*-Si:H increases.[73] It has been accepted widely that the energy states of the SiH_n bonding are created far from the Fermi energy position and located deeply into the valence band.[69,70,72,73] As a result, the valence-band top shifts with C_{total} due to the reduction in the DOS by the Si(3*p*)-H(1*s*) interaction.[69] The tight-binding calculation for *a*-Si:H also confirmed the shift of the valence-band position with C_{total}.[70] On the other hand, the conduction-band bottom is less affected by the presence of the SiH_n bonding states, and the inverse photoemission experiment showed no variation in the conduction-band edge position with H.[74]

In our model, the band-gap widening in *a*-Si:H, owing to the change in the valence-band position, has been reproduced by the shift of the whole $\varepsilon_{a\text{-Si:H}}(E)$ toward higher energies with increasing C_{SiH} and C_{SiH_2}. An important observation is the difference in the energy shift coefficients for C_{SiH} and C_{SiH_2}; i.e., k_1 and k_2. As confirmed from Fig. 8, $k_1 = 9.4$ meV/at.% is much larger than $k_2 = 4.0$ meV/at.%. Although the values of k_1 and k_2 vary according to A_{SiH} and A_{SiH_2}, our result suggests that the SiH_2 bonding state is more localized and the interaction with the valence-band top is weaker, compared with the SiH bonding state, as reported previously.[69]

So far, the SiH_2 bonding state has been reported to show a strong correlation with the photoinduced degradation in *a*-Si:H.[14–18] The finding in this study further suggests that the degradation phenomenon occurs within the SiH_2-microvoid structure. Nevertheless, the defect density created by the photoinduced degradation is of the order of ∼10^{17} cm^{-3} (Refs. 15 and 17) and is far smaller than C_{SiH_2} (∼10^{21} cm^{-3}). Thus it appears that specific local atomic structures with a density much smaller than C_{SiH_2} are involved in the actual photoinduced structural change. It has been reported that the presence of the ∼2080 cm^{-1} IR peak increases the Urbach edge parameter.[13] From this result, we suggest that the SiH_2-microvoid structure enhances the formation of the tail state near the valence band.

VI. CONCLUSION

The dielectric function and SiH_n local bonding states of *a*-Si:H layers deposited at different substrate temperatures of $T_s = 80$–$310\,^{\circ}$C have been determined. We find that the amplitude of the *a*-Si:H dielectric function $\varepsilon_{a\text{-Si:H}}(E)$ decreases with increasing the SiH_2 content and is completely described by the density of the SiH_2 bonding state in *a*-Si:H. From this result, we concluded that the formation of the microvoids terminated with SiH_2 bonds occurs in the *a*-Si:H network with increasing the SiH_2 content or decreasing T_s. For the variation of the SiH bonding state, on the other hand, the amplitude of $\varepsilon_{a\text{-Si:H}}(E)$ shows a quite small change, indicating that the SiH local structure is embedded into the dense network structure. With increasing the SiH and SiH_2 contents, the whole *a*-Si:H

dielectric function is found to shift toward higher energies. From the above findings, we have established a dielectric function model by taking into account the two phenomena: (i) the SiH_2-microvoid formation that reduces the amplitude of $\varepsilon_{a\text{-Si:H}}(E)$ and (ii) the energy shifts of $\varepsilon_{a\text{-Si:H}}(E)$ induced by the SiH_n bonding states. The effective-medium approximation has been applied to express the microvoid formation in the *a*-Si:H network. Our model provides excellent fitting to $\varepsilon_{a\text{-Si:H}}(E)$ obtained using a wide variety of deposition conditions. From this result, we confirmed that the optical properties of *a*-Si:H in the visible/UV region are almost perfectly determined by the SiH and SiH_2 local network structures. As a result, we have developed a dielectric function model for $\varepsilon_{a\text{-Si:H}}(E)$ with only two variables of the SiH and SiH_2 contents.

---

[*]fujiwara@gifu-u.ac.jp

[1]For example, see R. A. Street, *Hydrogenated Amorphous Silicon* (Cambridge University Press, New York, 1991).

[2]W. E. Spear and P. G. Le Comber, Solid State Commun. **17**, 1193 (1975).

[3]W. E. Spear and P. G. Le Comber, Philos. Mag. **33**, 935 (1976).

[4]D. E. Polk, J. Non-Cryst. Solids **5**, 365 (1971).

[5]D. E. Polk and D. S. Boudreaux, Phys. Rev. Lett. **31**, 92 (1973).

[6]D. Weaire, N. Higgins, P. Moore, and I. Marshall, Philos. Mag. B **40**, 243 (1979).

[7]W. Schülke, Philos. Mag. B **43**, 451 (1981).

[8]F. Wooten, K. Winer, and D. Weaire, Phys. Rev. Lett. **54**, 1392 (1985).

[9]For a review, see H. Fritzsche, Sol. Energy Mater. **3**, 447 (1980).

[10]G. D. Cody, C. R. Wronski, B. Abeles, R. B. Stephens, and B. Brooks, Solar Cells **2**, 227 (1980).

[11]D. Ewald, M. Milleville, and G. Weiser, Philos. Mag. B **40**, 291 (1979).

[12]G. F. Feng, M. Katiyar, J. R. Abelson, and N. Maley, Phys. Rev. B **45**, 9103 (1992).

[13]A. H. Mahan, P. Menna, and R. Tsu, Appl. Phys. Lett. **51**, 1167 (1987).

[14]E. Bhattacharya and A. H. Mahan, Appl. Phys. Lett. **52**, 1587 (1988).

[15]N. Nakamura, T. Takahama, M. Isomura, M. Nishikuni, K. Yoshida, S. Tsuda, S. Nakano, M. Ohnishi, and Y. Kuwano, Jpn. J. Appl. Phys. **28**, 1762 (1989).

[16]S. Guha, J. Yang, S. J. Jones, Y. Chen, and D. L. Williamson, Appl. Phys. Lett. **61**, 1444 (1992).

[17]S. Shimizu, M. Kondo, and A. Matsuda, J. Appl. Phys. **97**, 033522 (2005).

[18]H. Takatsuka, Y. Yamauchi, K. Kawamura, H. Mashima, and Y. Takeuchi, Thin Solid Films **506-507**, 13 (2006).

[19]P. D'Antonio and J. H. Konnert, Phys. Rev. Lett. **43**, 1161 (1979).

[20]A. H. Mahan, D. L. Williamson, B. P. Nelson, and R. S. Crandall, Solar Cells **27**, 465 (1989).

[21]A. H. Mahan, Y. Xu, D. L. Williamson, W. Beyer, J. D. Perkins, M. Vanecek, L. M. Gedvilas, and B. P. Nelson, J. Appl. Phys. **90**, 5038 (2001).

[22]A. J. Leadbetter, A. A. M. Rashid, N. Colenutt, A. F. Wright, and J. C. Knights, Solid State Commun. **38**, 957 (1981).

[23]Y. J. He, M. Hasegawa, R. Lee, S. Berko, D. Adler, and A. L. Jung, Phys. Rev. B **33**, 5924 (1986).

[24]V. G. Bhide, R. O. Dusane, S. V. Rajarshi, A. D. Shaligram, and S. K. David, J. Appl. Phys. **62**, 108 (1987).

[25]J. C. Knights, G. Lucovsky, and R. J. Nemanich, J. Non-Cryst. Solids **32**, 393 (1979).

[26]A. H. M. Smets and M. C. M. van de Sanden, Phys. Rev. B **76**, 073202 (2007).

[27]J. B. Boyce and M. Stutzmann, Phys. Rev. Lett. **54**, 562 (1985).

[28]M. H. Brodsky, M. Cardona, and J. J. Cuomo, Phys. Rev. B **16**, 3556 (1977).

[29]J. C. Knights, G. Lucovsky, and R. J. Nemanich, Philos. Mag. B **37**, 467 (1978).

[30]G. Lucovsky, R. J. Nemanich, and J. C. Knights, Phys. Rev. B **19**, 2064 (1979).

[31]H. Shanks, C. J. Fang, L. Ley, M. Cardona, F. J. Demond, and S. Kalbitzer, Phys. Status Solidi B **100**, 43 (1980).

[32]W. B. Pollard and G. Lucovsky, Phys. Rev. B **26**, 3172 (1982).

[33]M. Cardona, Phys. Status Solidi B **118**, 463 (1983).

[34]J. D. Ouwens and R. E. I. Schropp, Phys. Rev. B **54**, 17759 (1996).

[35]J. A. Reimer, R. W. Vaughan, and J. C. Knights, Phys. Rev. Lett. **44**, 193 (1980).

[36]W. E. Carlos and P. C. Taylor, Phys. Rev. B **26**, 3605 (1982).

[37]J. Baum, K. K. Gleason, A. Pines, A. N. Garroway, and J. A. Reimer, Phys. Rev. Lett. **56**, 1377 (1986).

[38]K. K. Gleason, M. A. Petrich, and J. A. Reimer, Phys. Rev. B **36**, 3259 (1987).

[39]R.E. Norberg, D. J. Leopold, and P. A. Fedders, J. Non-Cryst. Solids **227-230**, 124 (1998).

[40]P. A. Fedders, D. J. Leopold, P. H. Chan, R. Borzi, and R. E. Norberg, Phys. Rev. Lett. **85**, 401 (2000).

[41]W. B. Jackson, S. M. Kelso, C. C. Tsai, J. W. Allen, and S.-J. Oh, Phys. Rev. B **31**, 5187 (1985).

[42]A. R. Forouhi and I. Bloomer, Phys. Rev. B **34**, 7018 (1986).

[43]S. Adachi, *Optical Properties of Crystalline and Amorphous Semiconductors: Materials and Fundamental Principles* (Kluwer Academic, Norwell, 1999).

[44]J. Leng, J. Opsal, H. Chu, M. Senko, and D. E. Aspnes, Thin Solid Films **313-314**, 132 (1998).

[45]H. R. Philipp, J. Phys. Chem. Solids **32**, 1935 (1971).

[46]D. E. Aspnes and J. B. Theeten, J. Appl. Phys. **50**, 4928 (1979).

[47]G. E. Jellison Jr. and F. A. Modine, Appl. Phys. Lett. **69**, 371 (1996); **69**, 2137 (1996).

[48]A. S. Ferlauto, G. M. Ferreira, J. M. Pearce, C. R. Wronski, R. W. Collins, X. Deng, and G. Ganguly, J. Appl. Phys. **92**, 2424 (2002).

[49]H. Fujiwara, M. Kondo, and A. Matsuda, J. Appl. Phys. **91**, 4181 (2002).

[50]G. E. Jellison Jr. and F. A. Modine, J. Appl. Phys. **76**, 3758 (1994).

[51]A. Matsuda, K. Nomoto, Y. Takeuchi, A. Suzuki, A. Yuuki, and J. Perrin, Surf. Sci. **227**, 50 (1990).

[52]H. Fujiwara, M. Kondo, and A. Matsuda, Jpn. J. Appl. Phys. **41**, 2821 (2002).

[53]H. Fujiwara, J. Koh, P. I. Rovira, and R. W. Collins, Phys. Rev. B **61**, 10832 (2000).

[54]H. Fujiwara, *Spectroscopic Ellipsometry: Principles and Applications* (Wiley, West Sussex, UK, 2007).

[55] A. A. Langford, M. L. Fleet, B. P. Nelson, W. A. Lanford, and N. Maley, Phys. Rev. B **45**, 13367 (1992).
[56] H. Fujiwara, Y. Toyoshima, M. Kondo, and A. Matsuda, Phys. Rev. B **60**, 13598 (1999).
[57] M. Niwano, J. Kageyama, K. Kurita, K. Kinashi, I. Takahashi, and N. Miyamoto, J. Appl. Phys. **76**, 2157 (1994).
[58] G. Lucovsky, Solid State Commun. **29**, 571 (1979).
[59] O. Grimal, D. P. Masson, L. Bertrand, and A. Yelon, Phys. Rev. B **49**, 10242 (1994).
[60] C. Manfredotti, F. Fizzotti, M. Boero, P. Pastorino, P. Polesello, and E. Vittone, Phys. Rev. B **50**, 18046 (1994).
[61] N. Maley, Phys. Rev. B **46**, 2078 (1992).
[62] H. Touir, K. Zellama, and J.-F. Morhange, Phys. Rev. B **59**, 10076 (1999).
[63] G. Amato, G. Della Mea, F. Fizzotti, C. Manfredotti, R. Marchisio, and A. Paccagnella, Phys. Rev. B **43**, 6627 (1991).
[64] A. H. M. Smets, W. M. M. Kessels, and M. C. M. van de Sanden, Appl. Phys. Lett. **82**, 1547 (2003).
[65] Y. J. Chabal and C. K. N. Patel, Phys. Rev. Lett. **53**, 210 (1984).
[66] Y. J. Chabal and C. K. N. Patel, Phys. Rev. Lett. **53**, 1771 (1984).
[67] J. D. Joannopoulos and M. L. Cohen, Phys. Rev. B **7**, 2644 (1973).
[68] W. Y. Ching and C. C. Lin, Phys. Rev. B **18**, 6829 (1978).
[69] W. Y. Ching, D. J. Lam, and C. C. Lin, Phys. Rev. B **21**, 2378 (1980).
[70] D. A. Papaconstantopoulos and E. N. Economou, Phys. Rev. B **24**, 7233 (1981).
[71] P. Lautenschlager, M. Garriga, L. Viña, and M. Cardona, Phys. Rev. B **36**, 4821 (1987).
[72] K. H. Johnson, H. J. Kolari, J. P. de Neufville, and D. L. Morel, Phys. Rev. B **21**, 643 (1980).
[73] B. von Roedern, L. Ley, and M. Cardona, Phys. Rev. Lett. **39**, 1576 (1977).
[74] W. B. Jackson, S.-J. Oh, C. C. Tsai, and J. W. Allen, Phys. Rev. Lett. **53**, 1481 (1984).